Multidisciplinary approach to cylindrical anisotropic metamaterials

2011 New J. Phys. 13 103034

(http://iopscience.iop.org/1367-2630/13/10/103034)

New Journal of Physics
The open-access journal for physics

Multidisciplinary approach to cylindrical anisotropic metamaterials

Jorge Carbonell, Daniel Torrent, Ana Díaz-Rubio and José Sánchez-Dehesa[1]

Wave Phenomena Group, Departamento de Ingeniería Electrónica, Universidad Politécnica de Valencia, Camino de Vera s/n, 46022 Valencia, Spain
E-mail: jorcarol@upvnet.upv.es, datorma1@upvnet.upv.es, andiaru@upvnet.upv.es and jsdehesa@upvnet.upv.es.

New Journal of Physics **13** (2011) 103034 (20pp)
Received 22 July 2011
Published 24 October 2011
Online at http://www.njp.org/
doi:10.1088/1367-2630/13/10/103034

Abstract. Anisotropic characteristics of cylindrically corrugated microstructures are analyzed in terms of their acoustic and electromagnetic (EM) behavior paying special attention to their differences and similarities. A simple analytical model has been developed using effective medium theory to understand the anisotropic features of both types of waves in terms of radial and angular components of the wave propagation velocity. The anisotropic constituent parameters have been obtained by measuring the resonances of cylindrical cavities, as well as from numerical simulations. This permits one to characterize propagation of acoustic and EM waves and to compare the fundamental anisotropic features generated by the corrugated effective medium. Anisotropic coefficients match closely in both physics fields but other relevant parameters show significant differences in the behavior of both types of waves.

[1] Author to whom any correspondence should be addressed.

Contents

1. Introduction

Over the last decade, a great deal of effort has concentrated on the possibility of controlling wave propagation phenomena based on the use of microstructured devices, usually termed 'metamaterials' [1]. This broad area of research covers aspects from theory of wave propagation in complex media to micro- and nano-fabrication techniques (with their corresponding operation frequencies), and even different disciplines or application fields such as acoustics or electromagnetism. One of the core targets of this effort is related to the so-called 'total control' of wave propagation. Towards this goal, a number of unusual phenomena have been investigated, which in principle cannot be achieved with 'natural' materials: negative refraction, super-resolution focusing or cloaking [2–4]. One of the foundations of this field is the use of artificial microstructures made of 'small' (as compared to the operation wavelengths) elements or inclusions as unitary constituents that possess a proper geometrical arrangement and characteristic parameters. They are usually, even though not necessarily, implemented with periodic and/or multilayered structures [5]. These devices operate in the 'long-wavelength' regime, where the operation wavelength is much larger than the characteristic unit cell dimensions of the constituents. Additionally, one of the characteristic features in the background of some interesting phenomena, such as wave channeling and routing or magnification, is wave propagation anisotropy [6]. Anisotropic phenomena have been largely investigated both in acoustics [7–9] and in electromagnetism [10, 11]. The control of anisotropic propagation is a key condition to allow a number of applications, which can cover a broad spectrum of areas, from directive antennas [12] to cloaking devices [13, 14].

Both the disciplines, acoustics and electromagnetism, are governed by different wave propagation equations that, respectively, describe sound pressure and electromagnetic (EM) field distributions. Key parameters that allow the solution of these problems are, on the one hand, mass density and bulk modulus and, on the other hand, permittivity (ε) and permeability (μ) functions. Equivalencies have already been pointed out between both fields that necessarily have to take into account that the sound problem is a scalar one, whereas the light problem is a vector one [15].

Corrugated surfaces and devices based on corrugations are a direct link between both areas for an integrated and multidisciplinary approach, since they have been analyzed from each

point of view for a long time. Nevertheless, previous works did not focus specifically on the study of the long-wavelength regime and homogenization issues regarding this type of media. It has not been common also to study these micro-structured surfaces simultaneously from both application fields. Traditionally, corrugated structures have been a means of generating slow waves at microwaves [16–18] and, more recently, terahertz frequencies [19]. Moreover, part of the acoustic terminology has been used in electromagnetism for the study of periodic corrugated propagation media with intense studies on the so-called *hard* and *soft* surfaces [20]. Also, corrugated surfaces were studied in the past from an acoustic point of view [21, 22]. More recently, experimental investigations have analyzed propagation of sound waves on periodically corrugated metallic plates [23].

In this paper, we report a direct and comparative approach to periodic corrugated structures with cylindrical symmetry from both application fields. Several sample structures are analyzed and characterized to obtain a double (acoustic and EM) anisotropic response in terms of wave propagation. This study reveals that there are similarities and differences between both wave problems, with the common feature of generating anisotropic propagation media. The paper is organized as follows. Firstly, in section 2, the samples forming cylindrical resonant metallic cavities are experimentally characterized with two different measurement setups. This allows us to analyze the acoustic and EM responses. In particular, resonant modes of the cavities are investigated paying special attention to their variation due to the anisotropy generated by introducing a corrugated surface on the bottom of the cavity. Comparative results are expressed in terms of measured resonant modes as a function of frequency. Secondly, in section 3, the previous experimental results are analyzed from theoretical and numerical points of view, taking advantage of a previously reported analysis on acoustics [24]. The solutions of the two problems possess similarities and differences that are basically analyzed in terms of extracted constituent parameters. They help one to understand the anisotropic behavior derived from the microstructured propagation medium. Finally, some conclusions summarize the main findings of this work.

2. Experimental characterization

Corrugated structures are perfect candidates to perform a multidisciplinary study of anisotropic propagation media, since they have been used in both application fields for a long time. In principle, frequency ranges associated with the audible range (20 Hz–20 kHz) compare to an equivalent microwave frequency range (17.5 MHz–17.5 GHz), taking into account that identical wavelength ranges apply in both fields, with $\lambda_{\min} = 17.16\,\text{mm}$ and $\lambda_{\max} = 17.16\,\text{m}$. This equivalence is found from the fact that the sound propagation speed in air is $v_s = 341\,\text{m s}^{-1}$ and light propagation speed in vacuum (and approximately in air) is $c_0 = 3 \times 10^8\,\text{m s}^{-1}$. Corrugated structures are basically implemented with a periodically varying stepped surface, which is patterned on a metal plate.

An example of a circular metallic cavity with a cylindrically corrugated bottom surface is displayed in figure 1. The structure is patterned on two separate aluminum plates. The cavity is open to allow viewing the inside, and the closing flat metallic surface is also displayed. It permits one, through perforated apertures, to excite and probe this resonant element from different positions. In our study this is done with microwave connectors and a set of loudspeakers and microphones, to respectively characterize the EM and acoustic responses of the same cavity. The EM probing and excitation elements are also displayed in the same figure 1. A vector

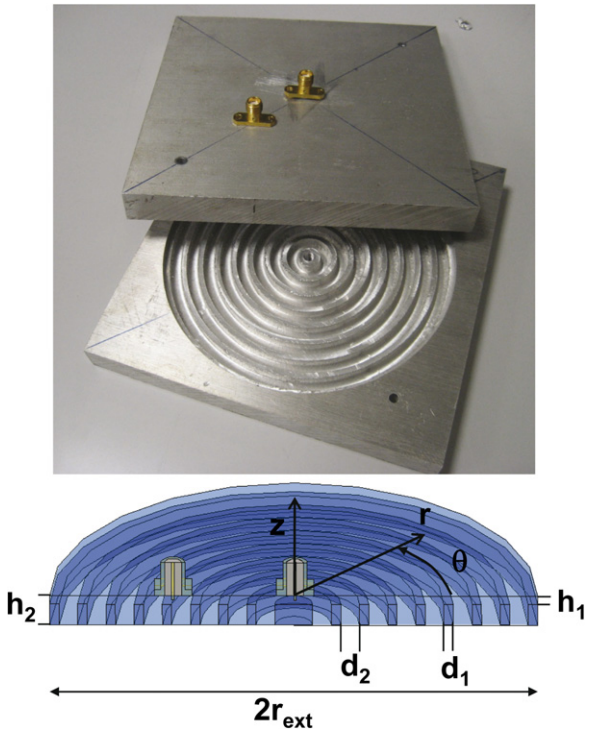

Figure 1. Upper panel: corrugated metallic cavity (open, which allows viewing the interior) and EM coaxial connectors for excitation and probing; lower panel: schematic cross-sectional view of the prototype device with characteristic dimensions and excitation-probing microwave elements. The z-direction is perpendicular to the metallic corrugated plate defining the xy plane.

network analyzer gives the EM response as a transmission coefficient (from the excitation to the probe connectors) expressed as a function of frequency. A standard calibration has been performed to eliminate the systematical measurement errors. The acoustic response is obtained as a measure of the sound pressure intensity which is a function of the excitation frequency of the loudspeaker.

Several samples have been fabricated based on the device of figure 1; they differ from each other only in the variable parameter h_1, the free height above the corrugations [24]. Additionally, a hollow cavity with no corrugated surface is also characterized as a reference device. All cavities have identical radius ($r_{\text{ext}} = 52$ mm) and total height ($h_2 = 7$ mm). Finally, a normalized height h_1/h_2 is used for analysis purposes. It is important to underline that the same samples have been characterized in both measurement setups. In both situations, a long-wavelength regime applies, with radial periodicity of the structures ($d = d_1 + d_2 = 2 + 4 = 6$ mm) much smaller than the operation wavelengths. Let us note that the equivalence can also be established between the operational bandwidths in which the structures have been analyzed from both fields of application. In our case and, due to the geometry of our samples, the employed frequency ranges are 1–5 kHz for the acoustic waves and 1–5 GHz for the microwave experiments. They cover similar wavelength ranges from approximately $\lambda_{\text{min}} = 60$ mm to $\lambda_{\text{max}} = 340$ mm.

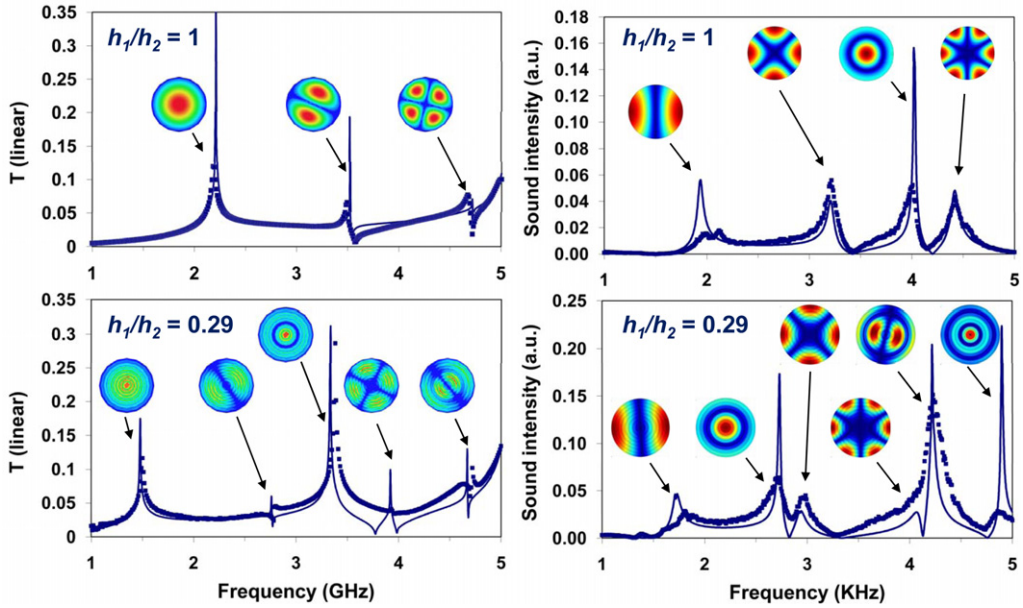

Figure 2. Resonant frequencies displayed as measured (with symbols) and simulated (with lines) field intensities as a function of frequency. Left panels display the EM case; right panels display acoustic results. Upper panels correspond to $h_1/h_2 = 1$ (empty cavity) and lower panels correspond to a corrugated cavity with $h_1/h_2 = 0.29$. Graphic insets display the resonant field patterns for each corresponding mode/frequency.

2.1. Sample transmission spectra

An experimental characterization of the cavity samples, combined with theoretical and numerical results, can provide an insight into the anisotropic features associated with wave propagation. We have analyzed the resonant modes of the closed cavities, with the purpose of inferring propagation parameters associated with the unbounded media. Excitation and probe positions are not exactly the same in both measurements. For the EM waves, connectors are located approximately at the cavity center and at a mid-point between the center and the external face of the cavity (see figure 1(b)). For the acoustic waves, microphones are located alternatively at different positions to measure, respectively, modes with different types of symmetries [24]. A loudspeaker feeds the cavity through an upper aperture located near its external radius.

The transmission spectra are summarized in figure 2, where panels display the experimental results for both types of waves. Left panels display, for the EM case, the transmission coefficient measured between the probe and excitation connectors. This is a normalized transmission coefficient which is proportional to the electric field intensity inside the cavity at the connector positions. Right panels display sound pressure intensity as measured with a microphone when the cavity is fed with a broadband noise generated by a loudspeaker. It is measured in arbitrary units and is proportional again to the field intensity at the microphone position. Therefore, these two measurements can be a means of comparing the resonant frequencies of the cavities for each setup. The results for the reference structure

(empty cavity—sample 4) and the cavity with deeper corrugations (minimum ratio $h_1/h_2 = 0.29$—sample 1) are displayed.

A first qualitative analysis of these results gives us a certain number of indications. The main observable result is the red shift of the resonant frequencies derived from the inclusion of the cylindrical corrugations in the cavity. This affects all resonant modes in the EM case that are shifted to lower frequency values. The frequency displacement is not homogeneous for all the measured modes. Additionally, frequency order of these modes is not equal for both cavities (empty and corrugated). In the acoustic case, measurements are carried out with a probe (microphone) at a non-central position in the cavity. This allows all modes to be measured with different relative intensities. The monopolar resonance ($m = 0$) is clearly shifted to lower frequencies as the ratio h_1/h_2 decreases. Nevertheless, the other modes ($m = 1, 2, 3$) are less affected by the introduction of the corrugation. Also comparing both regimes, note that relative positions of the different modes are not exactly the same; in particular, the first two modes have swapped positions. The first acoustic resonance of the reference cavity (upper right panel of figure 2) presents a split peak that should be attributed to imperfections of the measurement setup and possible fabrication and assembly tolerances.

3. Theory of cylindrical anisotropic structures

Our theoretical approach is based on the characterization of the samples through an effective medium theory (homogenization). Effective permittivity and permeability values can be associated with the EM wave propagation in the effective medium forming the cavity. In parallel, effective values of the bulk modulus and mass density can describe how sound waves can propagate in the effective medium filling the resonant cavity. Effective medium considerations are justified in both cases, since operation wavelengths are at least 10 times as high as the radial periodicity of the microstructure. Some effective parameter values can be extracted from the measured resonant frequencies of the cavities by first analyzing the field expressions for the closed cavities. The samples are modeled from the EM point of view for TM^z waves. This polarization configuration is equivalent to the scalar solution of the acoustic problem for the same sample. The fact that h_2 is small precludes the possibility of having TE solutions. Let us also note that from the EM point of view, image theory predicts that the solution of the cavity problem is identical to the case of a double height $2h_2$ cavity with a perfect electric symmetry boundary applied to the central plane of the metallic cavity. The total cavity is composed of the real cavity plus the image cavity having an upper corrugated surface. This double height cavity has identical behavior in its lower half than the real cavity.

Both problems share the wave nature of the respective solutions to a common tensor equation, i.e. the Helmholtz equation. It can be expressed in cylindrical coordinates for anisotropic media [25] respectively for EM (electric field) and acoustic (sound pressure) waves as:

$$\frac{1}{r}\frac{\partial}{\partial r}\left(\frac{r}{\mu_\theta}\frac{\partial E_z}{\partial r}\right) + \frac{1}{r^2\mu_\mathrm{r}}\frac{\partial^2 E_z}{\partial \theta^2} + \omega^2\varepsilon_z E_z = 0, \tag{1}$$

$$\frac{1}{r}\frac{\partial}{\partial r}\left(\frac{r}{\rho_\mathrm{r}}\frac{\partial P}{\partial r}\right) + \frac{1}{r^2\rho_\theta}\frac{\partial^2 P}{\partial \theta^2} + \omega^2 B^{-1} P = 0, \tag{2}$$

Table 1. Comparative relations and parameters to solve the two-dimensional EM and acoustic wave problems in cylindrical coordinates. Relevant anisotropic parameters are ordered according to the correspondence between both application fields.

Field ψ	Boundary condition	Solution type	c_r	γ
P	$\frac{\partial P}{\partial n} = 0$	$\psi(r,\theta;\omega) = \sum_n A_n J_{\gamma n}$	$\sqrt{B/\rho_r}$	$\sqrt{\rho_r/\rho_\theta}$
	$\frac{\partial P}{\partial r}\big\|_{r=r_{ext}} = 0$	$\times \left(\frac{\omega r}{c_r}\right) \cos(m\theta + \phi_m)$		
$TM^z \rightarrow E_z$	$E_{\|\|} = 0;\ H_\perp = 0$		$\frac{1}{\sqrt{\varepsilon_z \mu_\theta}}$	$\sqrt{\mu_\theta/\mu_r}$
	$E\|_{r=r_{ext}} = 0$			
$TE^z \rightarrow H_z$	$E_{\|\|} = 0;\ H_\perp = 0$		$\frac{1}{\sqrt{\varepsilon_\theta \mu_z}}$	$\sqrt{\varepsilon_\theta/\varepsilon_r}$
	$\frac{\partial H}{\partial r}\big\|_{r=r_{ext}} = 0$			

where ω is the angular frequency. These equations can be subsequently adapted to each field type taking into account the necessary boundary conditions that hold. These boundary conditions are what basically make the difference between both wave problems.

Table 1 describes for each type of wave the corresponding boundary condition associated with the metallic walls, the common solution type for a cylindrical cavity and the anisotropic parameters that can be used to characterize the expected anisotropy. These effective parameters are listed by column so it is possible to see the crossed relation between both application fields.

The cylindrical EM TM^z problem has solutions given by the Bessel functions $J(x)$ [26]. In that work [26], the solution is developed for the empty cavity. In terms of analysis, this cavity problem is a three-dimensional one with z-invariance. This configuration causes that only the TM^z modes are supported as solutions and no TE^z modes are allowed. Resonant frequencies of the different modes are related to the zeros of the Bessel functions.

Alternatively, the sound problem has solutions given by the *derivatives* of the Bessel functions $J'(x)$, and this is due to the boundary condition applied to the metallic walls [24], considered a hard boundary condition (see table 1). In this case, resonant frequencies are related to the zeros of the *derivatives* of the Bessel functions.

Previous hypotheses on the solutions of the two cavity problems explain the basic differences between the bounded problems, i.e. in terms of resonance parameters. For example, this explains the different ordering of the resonant modes in the acoustic case in comparison with that of the EM case (see figure 2). Nevertheless, this study allows us to go one step further and recover some of the parameters related to the unbounded problems such as the propagation ones, i.e. effective medium parameters and dispersion diagrams. In particular, the target is analyzing anisotropic propagation characteristics where a number of similarities are demonstrated in the following.

Anisotropic propagation is basically characterized by a modification of the effective parameters related to the radial wave propagation direction. This was pointed out in the acoustic case [24] for radial speed of sound c_r, and that analysis is not repeated here. At the same time, this is concomitant with virtually no change of the angular component of the complementary magnitude c_θ. The vector nature of the EM problem causes a comparable situation to be established taking into account that TM^z waves have horizontally polarized H-field (with H_r and

H_θ components) and vertically polarized E-field (with an E_z component). Therefore, relevant parameters are in this case radial and angular permeability values (μ_r and μ_θ) and the vertical component of the permittivity (ε_z).

3.1. Parameter extraction from experimental results

An analytical approach based on a simplified assumption is our first route to address the anisotropy characterization due to cylindrical corrugations. This approach is based on the assumptions of previous works [24], and is now extended to the EM problem. The development of this model for the acoustic case is not repeated in this study but, for the sake of completeness of the multidisciplinary approach, the fundamental relations are recalled. The model is based on the analysis of a cylindrical multilayered structure, formed from two alternative types of layers. First, it assumes that the height ratio between the empty layers (denoted with subscript 2) and the corrugated layers (denoted with subscript 1) is translated to the effective permittivity values:

$$\varepsilon_1 h_1 = \varepsilon_2 h_2. \tag{3}$$

Taking into account that, in each single layer, the light velocity should be unchanged, and also that $c_1^2 = 1/\varepsilon_1\mu_1 = c_2^2 = 1/\varepsilon_2\mu_2 = c_0^2$, we have

$$\mu_2 h_1 = \mu_1 h_2. \tag{4}$$

It is worth noting that, although this assumption is based on a translation from a hypothesis of the acoustic problem [7, 8], a completely equivalent derivation can be performed from the impedance analysis of a parallel plate transmission line [26]. This is followed by a homogenization procedure [6] of the cylindrical multilayer structure to generate effective parameters basically taking into account the fraction of each zone (empty or corrugated) in the full structure. This gives

$$\mu_r = \frac{d\mu_1\mu_2}{d_1\mu_2 + d_2\mu_1}, \tag{5}$$

$$\mu_\theta = \frac{d_1\mu_1 + d_2\mu_2}{d}, \tag{6}$$

$$\varepsilon_z = \frac{d_1\varepsilon_1 + d_2\varepsilon_2}{d}. \tag{7}$$

If the assumptions in (3) and (4) are translated to (5)–(7), the following expressions can be obtained for the effective parameters in cylindrical coordinates:

$$\mu_r = \frac{d\mu_2}{d_1\frac{h_2}{h_1} + d_2}, \tag{8}$$

$$\mu_\theta = \frac{\mu_2}{d}\left(d_1\frac{h_1}{h_2} + d_2\right), \tag{9}$$

$$\varepsilon_z = \frac{\varepsilon_2}{d}\left(d_1\frac{h_2}{h_1} + d_2\right). \tag{10}$$

And it finally follows that

$$\gamma^2 = \frac{\mu_\theta}{\mu_r} = \frac{1}{d^2}\left(d_1\frac{h_1}{h_2}+d_2\right)\left(d_1\frac{h_2}{h_1}+d_2\right) = \frac{\rho_r}{\rho_\theta}. \tag{11}$$

Note that expression (11) completely coincides with the γ definition for the acoustic case, since it depends only on geometrical parameters of the microstructure. This anisotropy coefficient γ relates the radial wave propagation velocity c_r and the angular wave propagation speed c_θ:

$$c_\theta = \gamma c_r = c_0. \tag{12}$$

Note that according to the definition of γ, we also have only for the EM case:

$$\gamma = \sqrt{\mu_\theta \varepsilon_z} = n_{\text{eff}}, \tag{13}$$

with n_{eff} being the effective refractive index of the homogenized medium along the radial propagation direction. This simple model therefore predicts identical anisotropy coefficients for both problems.

An equivalent procedure to that one introduced in previous works [24] allows the experimental extraction of the anisotropy coefficient for each of the higher modes ($m > 0$), starting from the radial speed c_r obtained from the measured fundamental resonances ($m = 0$). This allows a comparison with the previously introduced analytical model. For the EM case, this speed is obtained through the following equation related to the first zero of $J_0(x)$:

$$c_r^{\text{EM}} = \frac{2\pi f_{\text{TM01}} r_{\text{ext}}}{2.405}, \tag{14}$$

which uses as input the measured resonant frequencies f_{TM01} of the fundamental mode of each cavity. In the acoustic case, the radial sound speed was given by the expression:

$$c_r^{\text{Ac}} = \frac{2\pi f_{m=0} r_{\text{ext}}}{3.832}, \tag{15}$$

Then, the anisotropy coefficient γ for the higher resonant modes is obtained by, respectively, solving numerically the transcendental equations:

$$J_{\gamma m}^{\text{EM}}\left(\frac{2\pi f_{\text{TM}m1} r_{\text{ext}}}{c_r^{\text{EM}}}\right) = 0, \tag{16}$$

$$J_{\gamma m}^{'\text{Ac}}\left(\frac{2\pi f_m r_{\text{ext}}}{c_r^{\text{Ac}}}\right) = 0, \tag{17}$$

where the product γm is not an integer number.

A summary of the values obtained for the different measured cavities is given in table 2. Note that radial speed decreases for higher corrugations (a smaller height ratio) up to a factor 2/3 for $h_1/h_2 = 0.29$. In the empty cavity case ($h_1/h_2 = 1$), this extracted radial speed is virtually equal to the background speed (c_0 or v_s). In particular for the normalized radial speeds, comparison of both experiments gives very similar results. Anisotropy coefficients γ_1

Table 2. Measured frequencies for the different resonant modes and extracted radial wave velocities and anisotropy coefficients.

	EM						Acoustic		
h_1/h_2	f_{TM01} (GHz)	c_r/c_0	f_{TM11} (GHz)	γ_1	f_{TM21} (GHz)	γ_2	c_r/v_s	γ_1	γ_2
0.29	1.50	0.6793	2.78	1.4790	3.93	1.4675	0.6725	1.58	1.55
0.43	1.73	0.7835	3.03	1.2853	4.21	1.2857	0.7982	1.30	1.25
0.57	1.91	0.8650	3.21	1.1567	4.38	1.1503	0.8713	1.15	1.16
1.00	2.19	0.9918	3.51	1.0168	4.71	1.0143	0.9971	1.00	1.00

and γ_2, equivalent to effective indices for EM waves as pointed out above, are calculated for each of the higher modes TM_{11} and TM_{21}. These values are compared to those of the first two acoustic modes [24]. These coefficients have very similar values for both higher modes. They follow the same decreasing trend as the height ratio is increased, down to the limit of 1 for the empty cavity case. An important conclusion from this comparison is that, despite the different operating conditions, we have obtained an analytical and experimental confirmation of the similar behavior of both types of waves in terms of their anisotropic propagation characteristics.

3.2. Parameter extraction from numerical simulations

In a first stage, we have simulated the characterized samples with a full-wave finite element method solver [27] that allows the twofold analysis. Figure 2 already displayed the simulated transmission spectra and compared them with the measured results. A reasonable comparison is there obtained in both experiments. It is also significant that the numerical results allow identifying additional modes hidden in the experimental acoustic transmission spectra (see the $q = 3$ mode for the $h_1/h_2 = 0.29$ sample). From those data, the variation of the resonant frequency of each mode can be plotted as a function of the height ratio. Figure 3 compares the measured and simulated frequencies of the different resonant mode types as a function of the height ratio.

Excellent agreement is observed between the simulated resonant frequencies and the measured ones. Anisotropy presents differences between the modes: the EM mode with higher radial order, TM_{02}, is more affected; this also happens with the $q = 0$ acoustic mode. Additionally, these results clearly confirm that the lower frequency modes with unitary radial order, $n = 1$, are equally affected by anisotropy.

In a second stage, a standard extraction technique [28] has been employed to retrieve the effective parameters of the homogenized structure from transmission and reflection coefficients. These coefficients are obtained for both fields, through the finite element method [27], by using an 'equivalent unit-cell' (see the inset of figure 4). Analyses are performed for the radial, as well as for the angular propagation directions. Extraction of effective parameters for a radial propagation direction proves that there are both electric and magnetic activities (see figure 4). These extracted parameters have a direct equivalence and closely correspond to the effective acoustic parameters. Each set of parameters is extracted from the same basic procedure applied to the respective acoustic [29] or EM [28] numerical results. The reported values are extracted at 1 kHz and 1 GHz, respectively, the lowest measured and simulated frequencies.

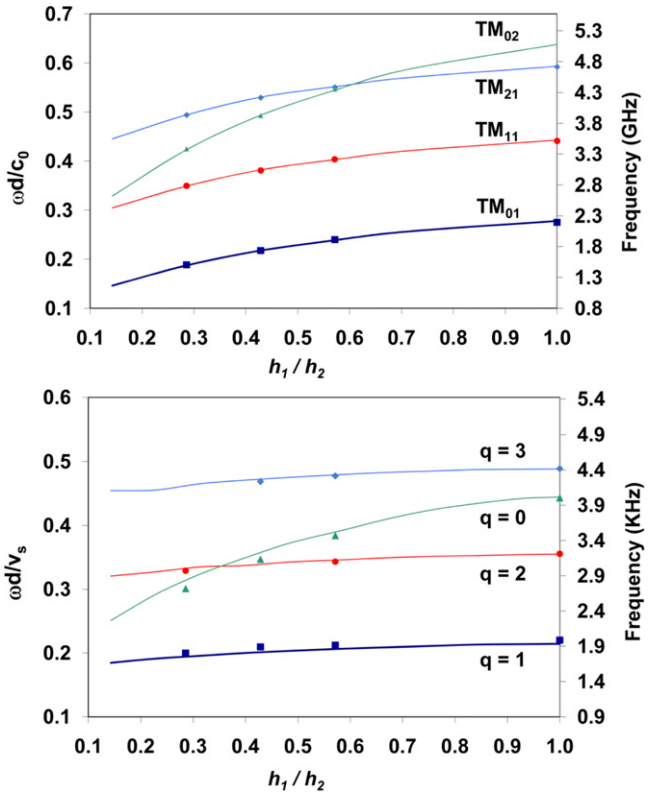

Figure 3. Measured (symbols) and simulated (lines) resonant frequencies for the different resonant modes in the corrugated cavities as a function of the ratio h_1/h_2, where h_2 is the total cavity height and h_1 is the free height above the corrugations (upper panel: EM results; lower panel: acoustic results).

From the EM point of view, magnetic activity is quite reduced, with relative permeability values (as a function of the corrugation height) positive and slightly smaller than one. This magnetic activity is exclusively due to the fact that the corrugation has a finite thickness [30]. Additional simulation results (not shown in this work) prove that parameter d_1 directly influences the magnetic response, which disappears when d_1 is tending to zero (no thickness corrugation). These results are based on full-wave simulations, but are in agreement with the equivalent circuit interpretation of a capacitive obstacle [30]. In this equivalence, the magnetic activity, due to the finite thickness of the obstacle-corrugation, is reported as a series inductance connected to the shunt capacitance associated with the height of the obstacle. This second element provides the fundamental capacitive behavior, generating hence the electric response. Figure 4 shows that the electric response (ε) is enhanced with decreasing height ratio h_1/h_2. An equivalent discussion can be established in terms of the effective acoustic parameters.

Figure 5 summarizes the parameter extractions performed as the h_1/h_2 ratio is increased from 0.14 up to 1 (empty cavity) from three points of view: measurements, numerical results and analytical model. Wave propagation velocity results are normalized with respect to the background wave speed (light in vacuum $c_0 = 3 \times 10^8\,\mathrm{m\,s^{-1}}$ and sound in air $v_s = 341\,\mathrm{m\,s^{-1}}$). The predicted anisotropy from the numerical results is relatively higher than that predicted

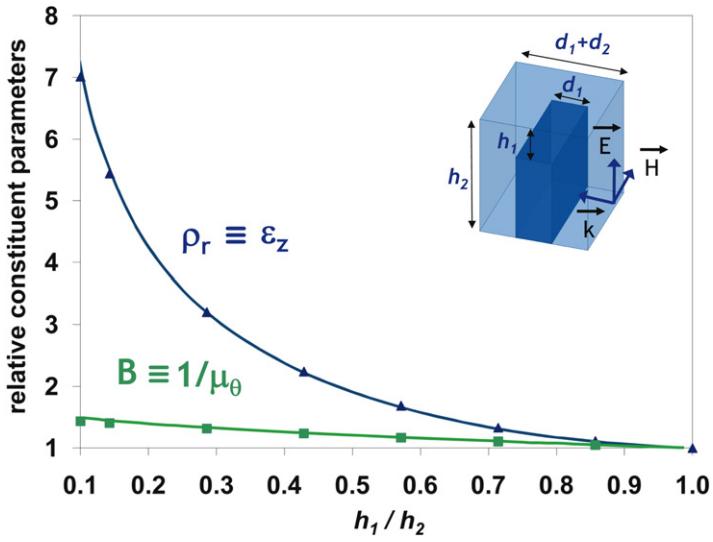

Figure 4. Extracted relative parameters for both acoustics (lines) and EM (symbols) and their equivalence relations for radial wave propagation. The inset displays the unit cell characteristic dimensions and EM excitation wave for the radial direction analysis.

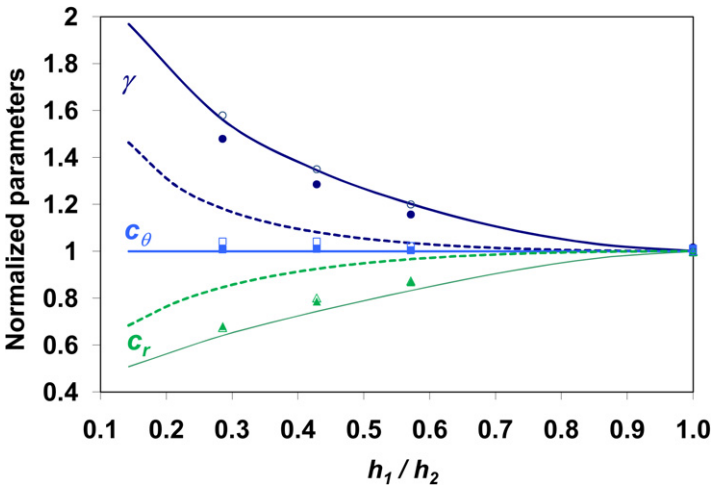

Figure 5. Extracted effective parameters from the measured results (EM: full symbols; acoustic: empty symbols), numerical simulations (both regimes, solid lines) and analytical model (both regimes, dashed lines). Normalized (with respect to c_0 and v_s) parameters represent the anisotropic coefficient γ, the angular propagation velocity c_θ and the radial propagation velocity c_r.

by the simple analytical model previously introduced. Actually, it is much closer to the parameters extracted from the measured frequencies. The values of γ follow a decreasing trend as h_1/h_2 is increased, which is consistent with the predicted behavior from the analytical model. Nevertheless, both curves (numerical and analytical) do not match exactly basically due to

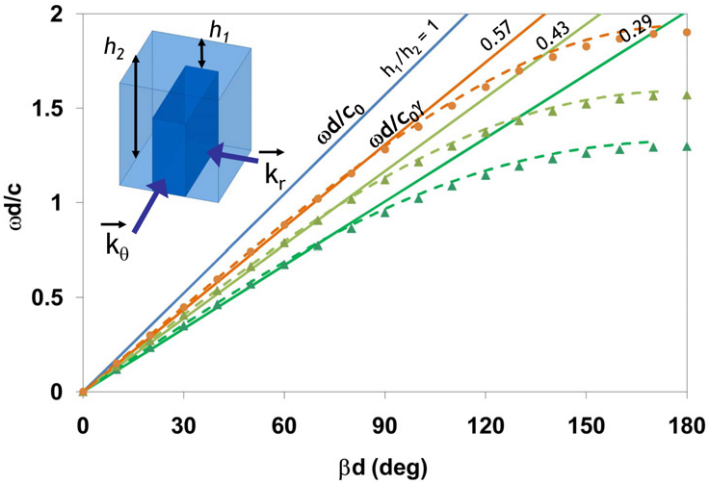

Figure 6. Normalized (with reference to c_0 or v_s respectively) dispersion diagram for radial and angular propagation constants. Symbols represent the full wave finite element method numerical results; solid lines are plotted from extracted parameters taking into account the anisotropy coefficient γ for the radial propagation direction; dashed lines are plotted from the analytical solution (see the appendix) of the eigenvalue unit cell problem (for the h_1/h_2 ratio of each resonant cavity).

the simplicity of the analytical model that rather gives a *qualitative* approximation. As in the acoustic case [31], the analytical model underestimates the measured results that are obviously better matched by the full-wave numerical results. The analytical model is based on two simple assumptions summarized in equations (3)–(7). These assumptions mean in fact modeling a single dominant mode propagating through the structure, instead of considering the multiple scattering components (i.e. evanescent modes) generated by the corrugation. The numerical results have been calculated again at the respective frequencies 1 kHz and 1 GHz. However, it is important to note that the EM experimental results do match very closely those measured in the acoustic case. Calculation of the experimental angular wave velocity is here also determined by $c_\theta = \gamma c_\mathrm{r}$. The fact that this c_θ result recovers the light velocity in vacuum c_θ or the sound speed in air v_s, with very minor errors, supports the extraction approach.

Finally, a further analysis of the effective medium parameters has been performed with the purpose of validating the homogenization approach in terms of quantifying the propagation anisotropy. Hence, the unbounded (periodic) medium has been analyzed in terms of its unit cell in the radial direction (see the inset of figure 6). Taking advantage of the numerical results, a dispersion diagram has been extracted by two methods. Firstly, an analytical solution has been developed from a mode matching technique (for details, see the appendix), whose results are plotted as dashed lines in figure 6. Secondly, a finite element solution has been generated by solving numerically the eigenvalue problem of a 'unit cell' and using the Bloch theorem with periodical boundary conditions on the side walls of the simulation domain. The two principal propagation directions have been analyzed corresponding to k_r and k_θ wave vectors (see the inset of figure 6). The phase difference between the parallel faces perpendicular to the wave vectors is varied and an eigenfrequency is obtained for each case (plotted with symbols).

For the k_θ direction, all curves lie on the same position and effectively match the 'air line' defining the radiation cone. Finite element solutions for the acoustical problem and the EM problem differ only by about 0.5% in terms of the calculated frequency points of the dispersion diagram. This difference is attributed to the numerical error in the simulations. Additionally, for the radial direction k_r, linear dispersion relations are plotted from the extracted values of figure 4 (numerical simulations based on transmission/reflection coefficients). It is evident that the model based on the extracted anisotropy coefficient can be compared accurately in the lower portion of the frequency spectrum with the eigenvalue or analytical solutions. The agreement is weaker as the frequency increases, basically due to the fact that at higher frequencies homogenization conditions no longer apply to this propagation structure. The deviation of the effective medium approach (solid lines in figure 6) from the full-wave approach (symbols and dashed lines in figure 6) is directly observable as the frequency increases, therefore giving an estimate of the maximum frequency at which the homogenization remains meaningful. On top of this result obtained from direct observation of the comparative graph, an upper limit could be set for the effective medium description. The upper frequency limit should be based on the fact that the microscopic spatial distributions of fields and polarization currents are slowly varying between adjacent unit cells. This is a key requisite for homogenization. With the condition $k_r d < 1$, the lattices can be considered as optically dense, although not quasi-static, and they can be adequately modeled by an equivalent continuous medium. At least, for the worst case scenario ($h_1/h_2 = 0.29$), the $k_r d < 1$ condition is fulfilled up to a normalized frequency of $\omega d/c = 0.55$. This value is approximately equivalent to $f = 5\,\mathrm{GHz}$ for the EM case and $f = 6\,\mathrm{kHz}$ for the acoustic case.

3.3. Loss analysis in anisotropic structures

The main drawback associated with anisotropy generated by corrugated surfaces in both acoustic and EM waves is the loss increase concomitant with the 'anisotropy increase'. The higher the corrugation heights, the higher the losses in wave propagation. A first step in the analysis of the loss increase as a consequence of increasing anisotropy of the propagation medium formed by the corrugated structure, is linked to the extraction of the imaginary part of the propagation constant related to the attenuation of waves. The complex propagation constant can be defined, taking into account attenuation of the propagating wave, as $k = \beta - \mathrm{j}\alpha$, with the phase constant β already assessed in the previous section. The attenuation constant α reflects the amount of loss due to the non-ideal materials employed in the corrugated structure. In particular for the EM case, finite conductivity of aluminum in both the top and bottom plates and the corrugations cause there to be an intrinsic loss in the medium ($\sigma_{\mathrm{alu}} = 3.8 \times 10^7\,\mathrm{S\,m^{-1}}$ in the simulations). The amount of loss is calculated per unit cell from the full wave simulations and is summarized in figure 7. It is calculated from simulations corresponding to the fabricated samples with different ratios of h_1/h_2. It can be seen that, in the absence of corrugations, losses increase approximately as the square root of frequency, a behavior typically associated with the finite conductivity of metals at microwaves. Moreover, as the corrugations increase (lower h_1/h_2 ratios), the effect, in terms of loss, increases and is added to the intrinsic metallic loss.

The loss increase is in any case observable for both EM and acoustic waves and therefore an experimental assessment of this fact is now addressed. In the case of bounded cavities, it is directly observable through the estimation of the quality factors of the different resonances as

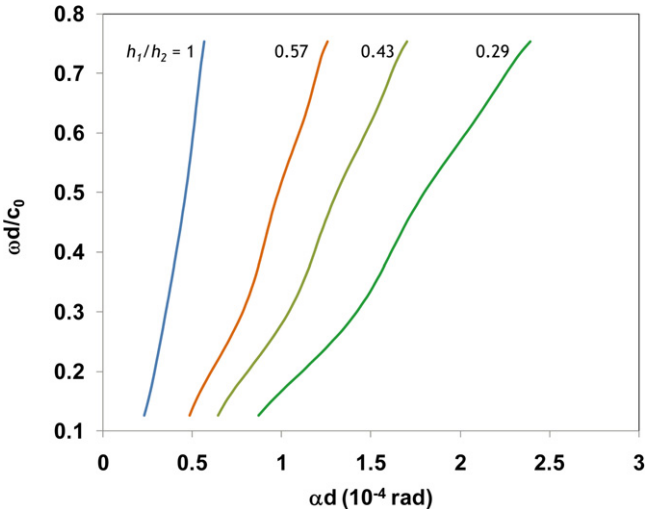

Figure 7. Normalized (with reference to c_0) dispersion diagram for radial EM attenuation constants. Solid lines are plotted from extracted parameters for different h_1/h_2 ratios.

Table 3. Estimated EM and acoustic Q-factors from measured and simulated resonant frequencies. Note that modes are ordered taking into account their respective resonance frequencies (normalized frequency value $\omega d/c$ in parentheses).

	EM				Acoustic			
	Measured		Simulated		Measured		Simulated	
h_1/h_2	$Q_{m=0}$	$Q_{m=1}$	$Q_{m=0}$	$Q_{m=1}$	$Q_{m=1}$	$Q_{m=0}$	$Q_{m=1}$	$Q_{m=0}$
0.29	113(0.19)	120(0.35)	1321(0.19)	1504(0.35)	37.8(0.20)	46.4(0.30)	41.3(0.19)	247.3(0.31)
0.43	243(0.22)	262(0.38)	1636(0.22)	1989(0.38)	37.2(0.21)	69.8(0.35)	46.4(0.20)	250.8(0.35)
0.57	479(0.24)	546(0.40)	1996(0.24)	2480(0.40)	34.3(0.21)	76.3(0.38)	52.1(0.21)	298.7(0.39)
1.00	725(0.28)	784(0.44)	3565(0.28)	4499(0.44)	46.1(0.22)	93.1(0.44)	66.5(0.22)	427.6(0.44)

h_1/h_2 is varying. It can be measured that Q-factors of the different resonances decrease with increasing anisotropy. A simple calculation is used to estimate very roughly the Q-factors of each resonance from the measured transmission spectra. The Q-factor estimation is performed with the ratio of the central resonance frequency to the fractional bandwidth:

$$Q = \frac{f}{\Delta f_{-3\mathrm{dB}}}. \tag{18}$$

The results are summarized in table 3. In both cases and as the ratio h_1/h_2 decreases, a significant reduction in Q-factors for the measured and simulated resonant frequencies can be deduced. This fact is a consequence of the metallic surface increase as corrugations have increased height and this is the main drawback of this approach. The evolution for the EM case is even more pronounced than that for the acoustic case.

Let us note that depending, on the one hand, on the exact position of the excitation and probing elements and, on the other, on the field pattern symmetry of the mode, it may be easier or not to calculate the Q-factor value from the measured and simulated spectra using equation (18). For modes with $m = 1, 2$, the resonances degenerate and it becomes difficult to perform a correct determination of the Q-factor. For that reason, the Q-factors from numerical results of the EM case have been directly obtained from eigenvalue simulations of a closed cavity. These values can therefore be considered as an upper threshold with respect to actual estimations. Nevertheless, for the experimental values and also for simulation spectra in the acoustic case, they have been estimated using equation (18). The results show a significant reduction in the measured quality factors with respect to the theoretical ones (especially in the EM case). The important differences between numerical and experimental results may be explained by a number of reasons: lower conductivity value of the actual aluminum employed for the samples, imperfect surface roughness, influence of the excitation and probing elements, and so on.

However, the same qualitative trend is clearly indicated by both measured and simulated quality factors. The quality factor values for each resonant mode are degraded with an increase of the corrugation heights. The loss increase is, in both cases, a fundamental drawback of these effective anisotropic metamaterials.

4. Conclusions

A multidisciplinary analysis of resonant cylindrical cavities with anisotropic characteristics has been performed from both acoustic and EM points of view. The approach employed is based on the characterization of the samples through an effective medium theory (homogenization). This procedure allows comparing directly effective medium parameters in terms of radial and angular wave propagation velocities between both application fields that define anisotropic behavior. An analytical model based on simple aspect geometrical ratios is used to assess the anisotropic characteristics of wave propagation media composed of cylindrical corrugated structures. This simple model qualitatively predicts the measured quantities in terms of the radial wave velocity and effective refractive index. Additionally, standard parameter extraction procedures confirm the qualitative behavior predicted by the analytical model. As has been stressed previously [15], the differences observed between acoustic waves and their EM counterparts in two dimensions mainly come from the differences in the boundary conditions of the bounded problems. These differences explain the observed behavior of the resonant parameters. However, in the case of the effective medium parameters corresponding to the unbounded media (propagation constants) an important conclusion is also that anisotropy effects derived from the cylindrical corrugation are quantitatively equivalent for both application fields. This multidisciplinary analysis opens the path for the design of devices based on an integrated approach to both types of phenomena.

Acknowledgments

The authors acknowledge financial support from the Spanish MICINN (TEC 2010-19751 and Consolider CSD2008-00066) and from the US Office of Naval Research (N000140910554). DT also acknowledges support from the program ‘Campus de Excelencia Internacional 2010 UPV’.

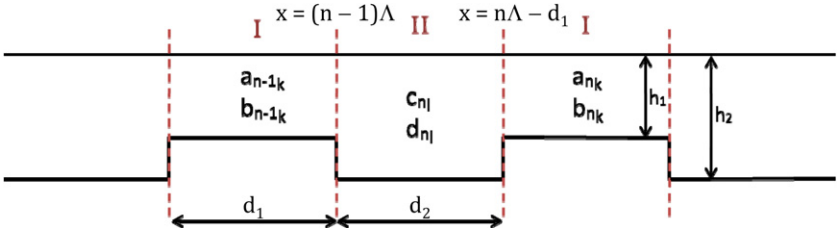

Figure A.1. Schematic diagram of a periodic structure made of alternative air layers with different heights and lengths forming the corrugated propagation medium.

Appendix

The unit cell to analyze is made of two alternative layers (air regions with different heights) bounded by metallic plates at the top and at the bottom. Region I has a height h_1 and a length d_1, while region II has a height h_2 and a length d_2 (see figure A.1).

The pressure field in each layer can be expressed as a combination of plane waves:

$$p^{\mathrm{I}}(x,z,\omega)=\sum_{k}(a_{nk}\,\mathrm{e}^{\mathrm{i}k_k^{\mathrm{I}}(x-nd)}+b_{nk}\,\mathrm{e}^{-\mathrm{i}k_k^{\mathrm{I}}(x-nd)})\Phi_k^{\mathrm{I}}(z),$$

$$p^{\mathrm{II}}(x,z,\omega)=\sum_{l}(c_{nl}\,\mathrm{e}^{\mathrm{i}k_l^{\mathrm{II}}(x-nd)}+d_{nl}\,\mathrm{e}^{-\mathrm{i}k_l^{\mathrm{II}}(x-nd)})\Phi_l^{\mathrm{II}}(z),$$

where

$$k_k^{\mathrm{I}}=\sqrt{\left(\frac{\omega}{c}\right)^2+\left(\frac{k\pi}{h_1}\right)^2},$$

and

$$k_l^{\mathrm{II}}=\sqrt{\left(\frac{\omega}{c}\right)^2+\left(\frac{l\pi}{h_2}\right)^2}$$

are the respective wave numbers, $\Phi_k^I(z)$ represent the vertical mode autofunctions and $d=d_1+d_2$. A mode matching analysis is employed. In the interface between the two layers, the pressure continuity and the pressure variation continuity conditions are imposed.

The pressure continuity condition imposes that the vertical mode projection of regions II and I over region I, in $0<z<h_1$, must be equal:

$$\int_0^{h_1}p^{\mathrm{I}}(x,z,\omega)|_{x_i}\Phi_s^I(z)\mathrm{d}z=\int_0^{h_1}p^{\mathrm{II}}(x,z,\omega)|_{x_i}\Phi_s^I(z)\mathrm{d}z.$$

Additionally, the pressure variation continuity forces the equality of the vertical mode projections over region II when $0<z<h_2$.

$$\int_0^{h_2}\left.\frac{\partial p^{\mathrm{I}}(x,z,\omega)}{\partial x}\right|_{x_i}\Phi_s^{\mathrm{II}}(z)\mathrm{d}z=\int_0^{h_2}\left.\frac{\partial p^{\mathrm{II}}(x,z,\omega)}{\partial x}\right|_{x_i}\Phi_s^{\mathrm{II}}(z)\mathrm{d}z.$$

The functions $\Phi_s^{\mathrm{I}}(z)$ and $\Phi_s^{\mathrm{II}}(z)$ are then defined as

$$\Phi_s^{\mathrm{I}}(z) = \begin{cases} (1/\sqrt{h_1})\cos\left(\dfrac{s\pi}{h_1}z\right), & s=0, \\ \sqrt{\dfrac{2}{h_1}}\cos\left(\dfrac{s\pi}{h_1}z\right), & s\neq 0, \end{cases}$$

$$\Phi_s^{\mathrm{II}}(z) = \begin{cases} 1/\sqrt{h_2}\cos\left(\dfrac{s\pi}{h_2}z\right), & s=0, \\ \sqrt{\dfrac{2}{h_2}}\cos\left(\dfrac{s\pi}{h_2}z\right), & s\neq 0 \end{cases}$$

Both conditions are imposed at the two interfaces ($x=(n-1)d$ and $x=nd-d_1$).

$$a_{(n-1)s}+b_{(n-1)s} = \sum_l G_{sl}\left(c_{nl}\,\mathrm{e}^{-\mathrm{i}k_l^{\mathrm{II}}d}+d_{nl}\,\mathrm{e}^{\mathrm{i}k_l^{\mathrm{II}}d}\right),$$

$$\sum_k k_k^{\mathrm{I}}G'_{sk}\left(a_{(n-1)k}-b_{(n-1)k}\right) = k_s^{\mathrm{II}}\left(c_{ns}\,\mathrm{e}^{-\mathrm{i}k_s^{\mathrm{II}}d}-d_{ns}\,\mathrm{e}^{\mathrm{i}k_s^{\mathrm{II}}d}\right),$$

$$a_{n_s}\,\mathrm{e}^{-\mathrm{i}k_s^{\mathrm{I}}\mathrm{d}_1}+b_{n_s}\,\mathrm{e}^{\mathrm{i}k_s^{l}d_1} = \sum_l G_{sl}\left(c_{nl}\,\mathrm{e}^{-\mathrm{i}k_l^{\mathrm{II}}d_1}+d_{nl}\,\mathrm{e}^{\mathrm{i}k_l^{\mathrm{II}}d_1}\right),$$

$$\sum_k k_k^{\mathrm{i}}G'_{sk}\left(a_{n_k}\mathrm{e}^{\mathrm{i}k_k^{\mathrm{I}}d_1}-b_{n_k}\mathrm{e}^{\mathrm{i}k_k^{\mathrm{I}}d_1}\right) = k_s^{\mathrm{II}}\left(c_{n_s}\mathrm{e}^{\mathrm{i}k_s^{\mathrm{II}}d_1}-d_{n_s}\mathrm{e}^{\mathrm{i}k_s^{\mathrm{II}}d_1}\right),$$

where $G_{sl}=\int_0^{h_1}\Phi_l^{\mathrm{II}}(z)\Phi_s^{\mathrm{I}}(z)\mathrm{d}z$ and $G'_{sk}=\int_0^{h_1}\Phi_k^{\mathrm{I}}(z)\Phi_s^{\mathrm{II}}(z)\mathrm{d}z$.

$$G_{sl} = \begin{cases} \sqrt{\dfrac{h_1}{h_2}}, & l=0,\ s=0, \\ 0, & l=0,\ s\neq 0, \\ \sqrt{\dfrac{2h_1}{h_2}}\,\mathrm{sinc}\left(\dfrac{lh_1}{h_2}\pi\right), & l\neq 0,\ s=0, \\ \sqrt{\dfrac{h_1}{h_2}}\left(\mathrm{sinc}\left(\dfrac{lh_1+sh_2}{h_2}\pi\right)+\mathrm{sinc}\left(\dfrac{lh_1-sh_2}{h_2}\pi\right)\right), & l\neq 0,\ s\neq 0, \end{cases}$$

$$G'_{sk} = \begin{cases} \sqrt{\dfrac{h_1}{h_2}}, & k=0,\ s=0, \\ \sqrt{\dfrac{2h_1}{h_2}}\,\mathrm{sinc}\left(\dfrac{sh_1}{h_2}\pi\right), & k=0,\ s\neq 0, \\ 0, & k\neq 0,\ s=0, \\ \sqrt{\dfrac{h_1}{h_2}}\left(\mathrm{sinc}\left(\dfrac{kh_2+sh_1}{h_2}\pi\right)+\mathrm{sinc}\left(\dfrac{kh_2-sh_1}{h_2}\pi\right)\right), & k\neq 0,\ s\neq 0. \end{cases}$$

This four-equation system can be rewritten as the following equations, which link the modes in three consecutive layers:

$$\begin{bmatrix} I_{(k,k)} & I_{(k,k)} \\ k_k^{\mathrm{i}} G'_{lk} & -k_k^{\mathrm{i}} G'_{lk} \end{bmatrix} \begin{pmatrix} a_{n-1} \\ b_{n-1} \end{pmatrix} = \begin{bmatrix} G_{kl}\, \mathrm{e}^{-\mathrm{i}k_l^{\mathrm{II}} d} & G_{kl}\, \mathrm{e}^{\mathrm{i}k_l^{\mathrm{II}} d} \\ I_{(l,l)} k_l^{\mathrm{II}}\, \mathrm{e}^{-\mathrm{i}k_l^{\mathrm{II}} d} & -I_{(l,l)} k_l^{\mathrm{II}}\, \mathrm{e}^{\mathrm{i}k_l^{\mathrm{II}} d} \end{bmatrix} \begin{pmatrix} c_n \\ d_n \end{pmatrix},$$

$$\begin{bmatrix} I_{(k,k)}\, \mathrm{e}^{-\mathrm{i}k_k^{\mathrm{i}} d_1} & I_{(k,k)}\, \mathrm{e}^{\mathrm{i}k_k^{\mathrm{i}} d_1} \\ k_k^{\mathrm{i}} G'_{lk}\, \mathrm{e}^{-\mathrm{i}k_k^{\mathrm{i}} d_1} & -k_k^{I} G'_{lk}\, \mathrm{e}^{\mathrm{i}k_k^{\mathrm{i}} d_1} \end{bmatrix} \begin{pmatrix} a_n \\ b_n \end{pmatrix} = \begin{bmatrix} G_{kl}\, \mathrm{e}^{-\mathrm{i}k_l^{\mathrm{II}} d_1} & G_{kl}\, \mathrm{e}^{\mathrm{i}k_l^{\mathrm{II}} d_1} \\ I_{(l,l)} k_l^{\mathrm{II}}\, \mathrm{e}^{-\mathrm{i}k_l^{\mathrm{II}} d_1} & -I_{(l,l)} k_l^{\mathrm{II}}\, \mathrm{e}^{\mathrm{i}k_l^{\mathrm{II}} d_1} \end{bmatrix} \begin{pmatrix} c_n \\ d_n \end{pmatrix}.$$

It is possible to assemble these two matrix equations by eliminating the term $\binom{c_n}{d_n}$ and write the relation between two similar consecutive regions:

$$\begin{pmatrix} a_n \\ b_n \end{pmatrix} = [M] \begin{pmatrix} a_{n-1} \\ b_{n-1} \end{pmatrix}.$$

According to the Bloch periodic wave condition, it can be rewritten as an eigenvalue problem:

$$[M] \begin{pmatrix} a_{n-1} \\ b_{n-1} \end{pmatrix} = \mathrm{e}^{-\mathrm{i}kd} \begin{pmatrix} a_n \\ b_n \end{pmatrix}.$$

Finally, the following equation gives the dispersion relation between $\boldsymbol{\beta}$ and $\boldsymbol{k}$:

$$\beta(\omega) = \frac{i}{d} \ln(\mathrm{e}^{-\mathrm{i}kd}).$$

References

[1] Engheta N and Ziolkowski R W 2006 *Metamaterials: Physics and Engineering Explorations* (New York: Wiley)
[2] Pendry J B, Schurig D and Smith D R 2006 *Science* **312** 1780
[3] Pendry J B 2000 *Phys. Rev. Lett.* **85** 3966
[4] Schurig D, Mock J J, Justice B J, Cummer S A, Pendry J B, Starr A F and Smith D R 2006 *Science* **314** 977
[5] Torrent D and Sanchez-Dehesa J 2009 *Phys. Rev. Lett.* **103** 064301
[6] Jacob Z, Alekseyev L V and Narimanov E 2006 *Opt. Express* **14** 8247
[7] Bradley C E 1994 *J. Acoust. Soc. Am.* **96** 1844
[8] Bradley C E 1994 *J. Acoust. Soc. Am.* **96** 1854
[9] Schoenberg M and Sen P N 1983 *J. Acoust. Soc. Am.* **73** 61
[10] Peng L, Ran L and Mortensen N A 2010 *Appl. Phys. Lett.* **96** 241108
[11] Carbonell J, Cervera F, Sanchez-Dehesa J, Arriaga J, Gumen L and Krokhin A 2010 *Appl. Phys. Lett.* **97** 231122
[12] Valero-Nogueira A, Alfonso E, Herranz J I and Baquero M 2007 *Microw. Opt. Technol. Lett.* **49** 1875
[13] Ni Y, Gao L and Qiu C 2010 *Plasmonics* **5** 251
[14] Huang Y, Feng Y and Jiang T 2007 *Opt. Express* **15** 11133
[15] Javier Garcia, de Abajo F, Estrada H and Meseguer F 2009 *New J. Phys.* **11** 093013
[16] Elliott R S 1954 *IRE Trans. Antennas Propag.* **2** 71
[17] Rotman W 1951 *Proc. Inst. Radio Eng.* **39** 952
[18] Goubau G 1950 *J. Appl. Phys.* **21** 1119

[19] Wang B, Jin Y and He S 2008 *Appl. Opt.* **47** 3694
[20] Kildal P S 1990 *IEEE Trans. Antennas Propag.* **38** 1537
[21] Giovannini L, Nizzoli F and Marvin A M 1992 *Phys. Rev. Lett.* **69** 1572
[22] Lakhtakia A, Varadan V K and Varadan V V 1985 *J. Acoust. Soc. Am.* **78** 2100
[23] Kundu T, Banerjee S and Jata K V 2006 *J. Acoust. Soc. Am.* **120** 1217
[24] Torrent D and Sanchez-Dehesa J 2010 *Phys. Rev. Lett.* **105** 174301
[25] Chew W 1999 *Waves and Fields in Inhomogeneous Media* (New York: Wiley)
[26] Harrington R F 1961 *Time-Harmonic Electromagnetic Fields* (New York: Wiley)
[27] Comsol AB (Sweden) 2010 *Comsol Multiphysics* (v.4.1) www.comsol.com
[28] Smith D R, Vier D C, Koschny T and Soukoulis C M 2005 *Phys. Rev.* E **71** 036617
[29] Fokin V, Ambati M, Sun C and Zhang X 2007 *Phys. Rev.* B **76** 144302
[30] Marcuvitz N 1986 *Waveguide Handbook* (London: Peregrinus IEEE)
[31] Torrent D and Sanchez-Dehesa J 2008 *New J. Phys.* **10** 023004